

PAPER

Error field impact on mode locking and divertor heat flux in NSTX-U

To cite this article: N.M. Ferraro *et al* 2019 *Nucl. Fusion* **59** 086021

View the [article online](#) for updates and enhancements.

Error field impact on mode locking and divertor heat flux in NSTX-U

N.M. Ferraro¹, J.-K. Park¹, C.E. Myers², A. Brooks¹, S.P. Gerhardt¹, J.E. Menard¹, S. Munaretto³ and M.L. Reinke⁴

¹ Princeton Plasma Physics Laboratory, Princeton, NJ, United States of America

² Sandia National Laboratory, Albuquerque, NM, United States of America

³ General Atomics, San Diego, CA, United States of America

⁴ Oak Ridge National Laboratory, Oak Ridge, TN, United States of America

E-mail: nferraro@pppl.gov

Received 25 January 2019, revised 11 April 2019

Accepted for publication 20 May 2019

Published 26 June 2019



Abstract

During the 2016 NSTX-U experimental campaign, locked modes in the plasma edge presented clear evidence of the presence of error fields. Extensive metrology and plasma response modeling with IPEC and M3D-C1 have been conducted to understand the various sources of error fields in NSTX-U as built in 2016, and to determine which of these sources have the greatest effect on the plasma. In particular, modeling finds that the error field from misalignment of the toroidal field (TF) coils may have a significant effect on the plasma. The response to the TF error field is shown to depend on the presence of a $q = 1$ surface, in qualitative agreement with experimental observations. It is found that certain characteristics of the TF error field present new challenges for error field correction. Specifically, the error field spectrum differs significantly from that of coils on the low-field side (such as the NSTX-U error field correction coils), and does not resonate strongly with the dominant kink mode, thus potentially requiring a multi-mode correction. Furthermore, to mitigate heat fluxes using poloidal flux expansion, the pitch angle at the divertor plates must be small ($\sim 1^\circ$). It is shown that uncorrected error fields may result in potentially significant local perturbation to the pitch angle. Estimates for coil alignment tolerances in NSTX-U are derived based on consideration of both heat flux and core resonant fields independently.

Keywords: tokamaks, error fields, NSTX-U

(Some figures may appear in colour only in the online journal)

1. Introduction

Error fields—non-axisymmetric magnetic fields present in tokamaks due to misaligned magnets or currents in external conducting structures—are well known to have deleterious effects on plasma performance. These effects can include mode locking [1, 2], rotation braking from neoclassical toroidal viscosity (NTV) [3, 4], and a reduction in thermal particle confinement (‘pump out’) [5–8]. Much work has been done on characterizing error fields on various tokamaks, and on correcting these error fields either using trim coils [9, 10] or by reducing errors in coil positioning and shape [11]. Fortunately, it is found that the plasma is often most sensitive to a particular error field distribution, with much lower

sensitivity to orthogonal distributions, in which case error field correction (EFC) can be effective with just a single trim coil set [12]. Models assuming that the plasma response is entirely due to a single error field distribution are known as ‘single-mode’ models, and are presently used successfully for EFC [13].

In NSTX-U, data obtained during the 2016 operations gave clear indications of the presence of error fields [14, 15]. The data further shows that the EFC coils were not able to fully correct these error fields in some circumstances. These observations are summarized in section 2.1. Given the inability to correct the error fields with the existing trim coils, significant effort has been made to understand the sources of error fields in NSTX-U as constructed in 2016, and to ensure that

the impact of error fields is reduced when NSTX-U resumes operation. This effort has involved extensive metrology, summarized in section 2.2, and plasma response calculations, described in section 3. Criteria for limiting the the potential consequences of the error fields both on core braking and heat flux to the divertor plates are used to inform the physics basis for tolerances in NSTX-U.

2. Characterization of error fields in NSTX-U

2.1. Evidence of error fields in NSTX-U

Observations from NSTX-U operations in 2016 revealed the signatures of significant error fields. In particular, it was found that many L-mode discharges were locked from the $q = 2$ surface outward. There was no evidence of a distinct locking event, and it is believed that the plasma edge was locked *ab initio*. The locked edge was not fatal; these plasmas typically continued to run through their intended duration unless disrupted by some other event such as loss of vertical position control. Error field correction using the NSTX-U mid-plane EFC coils was unsuccessful in preventing or unlocking the edge without causing the core also to lock, leading to disruption. This demonstrates the presence of multiple modes to which the plasma is sensitive, and indicates that the single-mode model is not valid in these cases.

Error field correction (EFC) in NSTX-U was impeded not only by the influence of multiple modes, but by a dramatic change in the optimal EFC phase over the duration of a discharge. Figure 1 shows the results of a scan of early-time EFC in 1 MW L-mode discharges in NSTX-U. In each case, a square EFC waveform of 600 A (1.2 kA-turns) was applied shortly after $t = 0$ at various phases. Using the core rotation as a proxy for the efficacy of a particular EFC phase, we infer that the optimum phase for EFC changes from $\phi = 200^\circ$ early in time to $\phi = 80^\circ$ in the flat top. This phase rotation constitutes a time (and/or scenario) dependent error field that would require a sophisticated EFC algorithm to correct. We note that the time of the phase change (roughly $t = 400$ ms) is nearly coincident with the formation of the $q = 1$ surface, which implies a significant $m/n = 1$ component of the error field.

2.2. Metrology

At the conclusion of the 2016 NSTX-U campaign, extensive metrology was conducted on the primary vertical field ('PF5') coils and the center stack assembly, which includes the central solenoid and the center rod of the toroidal field ('TF') coils. The relative positions of the inner face of the vessel wall and the center stack casing were measured using a ROMER Arm. The geometry of the outer face of the vessel wall was determined by adding 5/8" (15.875 mm), the nominal thickness of the stainless steel vessel wall, to the ROMER Arm

measurements of the inner face. These measurements are consistent with measurements from 2004, indicating that the vessel shape did not change substantially from that time.

Combining these measurements with ruler-based measurements of the distance between the PF5 and the outer vessel wall yields the PF5 radius as a function of toroidal angle. The $n = 1-3$ Fourier components of these measurements, shown in table 1, reveal shifts ($n = 1$ component) of roughly 0.5 cm of the PF5U and PF5L coils relative to the vertical axis of the ROMER Arm coordinate system, as well as significant non-circularities. Unlike the vacuum vessel, the PF5 coil shapes differ from measurements made in 2004. We believe that this difference is due to the fact that the radial restraints on the PF5 coils [11] were reconfigured during the upgrade to provide more freedom for the thermal expansion that is expected when operating 2 MA discharges in NSTX-U. At this time, the tilts of the PF5 coils have not been measured, but this activity is planned as part of the NSTX-U recovery project.

The shift and tilt of the TF center rod were determined by combining the ROMER Arm data with data additional metrology conducted after the center-stack (CS) assembly was removed from the machine using a FARO Laser Tracker. Ruler-based metrology was done before and after the removal of the CS assembly to verify that the TF position did not change during that process. The Laser Tracker was used to measure the relative positions of the inboard vertical divertor targets (IBDV) and the faces of the flags on the TF center rod. The locations of these elements are illustrated in figure 2. The TF center rod orientation in the ROMER Arm coordinate system was determined by using the two sets of IBDV measurements to transform the Laser Tracker measurements into the ROMER Arm coordinate system. The resulting position of the upper and lower TF flag faces in ROMER Arm coordinates defines the absolute shift and tilt of the TF center rod, shown in table 2. As can be seen, the TF rod is tilted and shifted relative to the center stack (CS) casing in which it is enclosed. The central solenoid (OH coil) alignment was not measured directly, but is believed to be well aligned with the TF rod.

2.3. Error field spectrum

The misalignments of the TF, PF, and OH coils result in an error field. For small shifts and tilts of the coils, the resulting error field will be linear in the shift and tilt and have toroidal mode number $n = 1$. A general method for calculating error fields from tilting and shifting magnetic coils is described in appendix A. It is found that for a coil that produces field \vec{B}^c in a coordinate system (r, ϕ, z) in which the coil is axisymmetric, the $n = 1$ component of that field in a coordinate system (R, φ, Z) such that (r, ϕ, z) is shifted by distance δ in direction φ_δ and rotated through an angle α about axis φ_α relative to (R, φ, Z) is

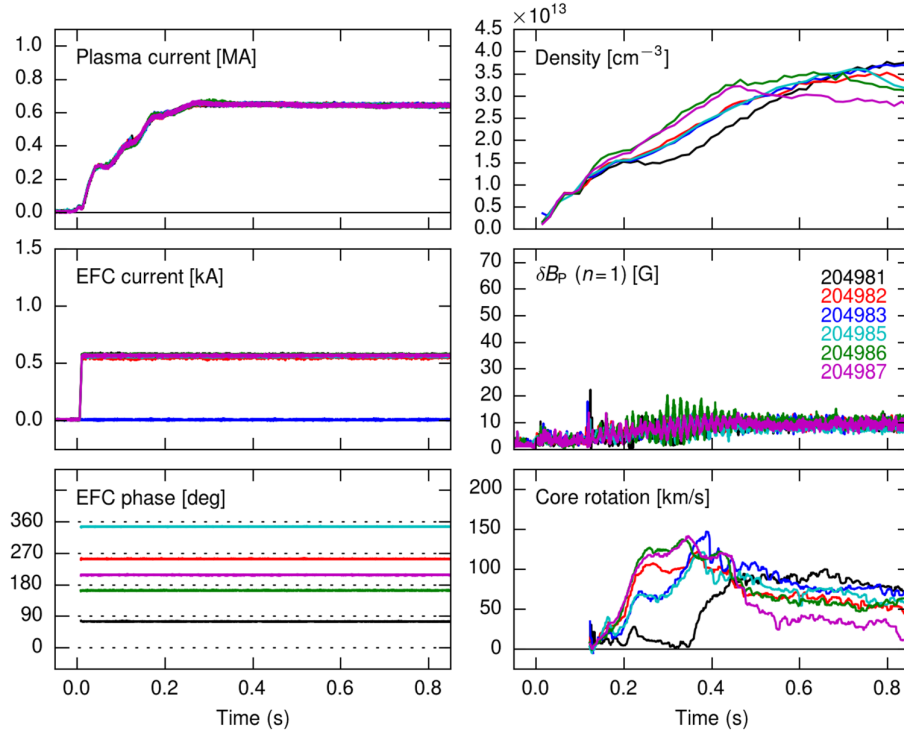


Figure 1. Scan of early-time externally applied error field correction (EFC) in 1 MW L-mode discharges in NSTX-U. The applied EFC current waveform is simply a square wave starting shortly after $t = 0$. The amplitude of the EFC is 600 A (1.2 kA-turns) in all cases, while the phase is varied from shot to shot. In the panel showing core rotation at the bottom right, a phase dependence of the plasma response is clearly visible (see the text for further details).

Table 1. Fourier components of the measured horizontal deviation from axisymmetry of the NSTX-U PF5 coils during the 2016 campaign.

Coil	$\delta R_{n=1}$ (mm)	$\varphi_{n=1}$ ($^\circ$)	$\delta R_{n=2}$ (mm)	$\varphi_{n=2}$ ($^\circ$)	$\delta R_{n=3}$ (mm)	$\varphi_{n=3}$ ($^\circ$)
PF5U	4.09	121	3.42	113	4.01	323
PF5L	6.19	55	4.09	11	9.45	292

$$\delta \vec{B} = \delta e^{i(\varphi - \varphi_s)} \begin{Bmatrix} -\partial_r B_r^c + i \frac{1}{R} B_\phi^c \hat{R} \\ - \left[i \frac{1}{R} B_r^c + \partial_r B_\phi^c \right] \hat{\varphi} \\ - \partial_r B_z^c \hat{Z} \end{Bmatrix} + \alpha e^{i(\varphi - \varphi_r)} \begin{Bmatrix} \left[i(R \partial_z B_r^c - Z \partial_r B_r^c) - \frac{Z}{R} B_\phi^c + i B_z^c \right] \hat{R} \\ \left[\frac{Z}{R} B_r^c + i(R \partial_z B_\phi^c - Z \partial_r B_\phi^c) - B_z^c \right] \hat{\varphi} \\ \left[-i B_r^c + B_\phi^c + i(R \partial_z B_z^c - Z \partial_r B_z^c) \right] \hat{Z} \end{Bmatrix} \quad (1)$$

to lowest order in δ and α . For small shifts and tilts of poloidal field coils, these results reproduce the results of La Haye and Scoville [18]. This error field can be written as an ideal MHD displacement $\delta \vec{B} = \nabla \times (\xi \times \vec{B})$ where

$$\vec{\xi} = \delta e^{\varphi - \varphi_s} (\hat{R} + i \hat{Z}) + \alpha e^{\varphi - \varphi_r} (i Z \hat{R} - Z \hat{\varphi} - i R \hat{Z}). \quad (2)$$

To understand the effect of an error field on the plasma, it is useful to consider the Fourier decomposition of the normal component of the error field in straight field-line magnetic

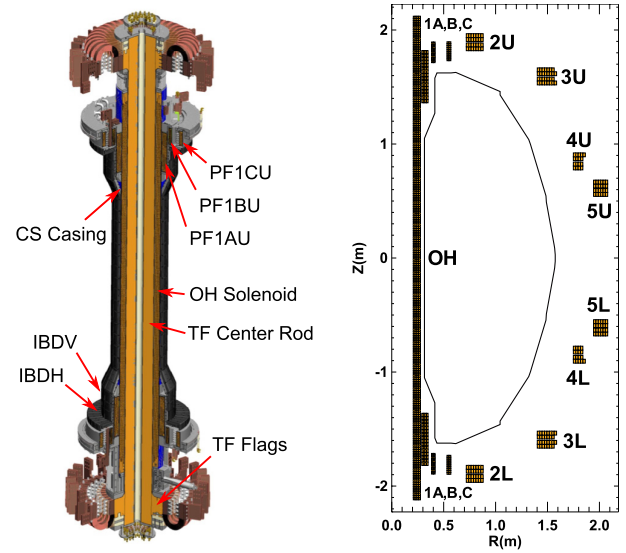


Figure 2. Left: model of the NSTX-U Center Stack assembly as designed for 2016 operation. Adapted with permission from [16]. Right: Schematic depicting locations of NSTX-U poloidal field coils. Reproduced courtesy of IAEA. Figure adapted from [17]. Copyright 2012 IAEA.

coordinates (ψ, θ, φ) based on the magnetic equilibrium in the absence of coil misalignments:

$$B_{mn}(\psi) = \frac{1}{(2\pi)^2 S} \iint d\varphi d\theta \mathcal{J} \delta \vec{B} \cdot \nabla \psi e^{im\theta - in\varphi}. \quad (3)$$

Table 2. The horizontal shift and tilt of the CS casing and TF center rod in the ROMER Arm coordinate system.

	Shift (mm)	Shift angle (°)	Tilt (mrad)	Tilt angle
CS casing	1.8	242°	0.15	156°
TF center rod	4.9	246°	1.15	206°

Here S is the surface area of the magnetic surface labeled by ψ ; θ and φ are the poloidal and toroidal angles, respectively, and $\mathcal{J} = [\nabla\psi \cdot \nabla\theta \times \nabla\varphi]^{-1}$. The impact of the error field on the plasma is often estimated by considering the magnitude of the resonant components of the error field—that is, the components for which $m = nq$ on a magnetic surface with safety factor q [5, 19]. More recently, it has been shown that a better measure of the impact of the error field is its overlap with the plasma response distribution that maximizes the formation of resonant currents [12, 20] or, more directly, by calculating the plasma response and directly evaluating the resulting resonant currents. This is done in section 3.

The error field spectrum depends on the coordinate system in which the field is measured. However, the resonant components of the field, which correspond directly to the width of the magnetic islands on the mode-rational surfaces [21], are not coordinate dependent. This has been shown to be true when considering different magnetic coordinate systems [22], and it is also true for arbitrary rigid displacements of a magnetic coordinate system (or equivalently, a rigid displacement of the plasma and magnets). This is discussed in more detail in section 3.3.

Here, we consider the error field generated by shifting or tilting individual coils with respect to the the ROMER Arm coordinates, which we take to define our reference coordinate frame. This error field depends linearly on the current in the misaligned coil, and is therefore scenario-dependent. The spectral decomposition defined by equation (3) also depends on the chosen axisymmetric equilibrium. Therefore we have considered several NSTX-U scenarios as part of this study. Here, we present two representative cases: a reconstruction from L-mode discharge 204077 at $t = 697$ ms, which is after the formation of the $q = 1$ surface; and a model H-mode discharge, here labeled 116313 after the NSTX discharge on which it is based. The L-mode discharge has $I_P = 620$ kA and $B_T = 0.6$ T. The model H-mode discharge has $I_P = 2$ MA and $B_T = 1$ T.

The error field spectrum (ignoring the plasma response) is relatively insensitive to the plasma shape, especially in the plasma core. Therefore we simply show the spectrum for a single case (204077 at $t = 697$ ms) in figure 3, using the $n = 1$ displacements given in tables 1 and 2. In this figure, the $-6 \leq m \leq -1$ components are plotted. Negative m values are shown because these components are resonant at surfaces with integer q values for a left-handed plasma (i.e. where the toroidal current and toroidal field are in opposite directions), which is the standard configuration for NSTX-U. For the error field from each coil misalignment individually, the negative m components have the same magnitude as the respective positive m components. The primary differences in error fields

among scenarios is the magnitude of the error field (due to differing coil currents) and the locations of the mode-rational surfaces. As can be seen, the TF error field is significantly larger than those from other coils, especially with respect to the $m/n = 1/1$ component of the field. The error field from the OH coil is significantly weaker than those of the other coils, and therefore is dropped from subsequent plots.

It is known that additional coil displacements will occur when the coils are powered due to electromagnetic forces [17]. For example, it is expected that twisting of the TF outer legs could lead to displacements of over 3 mm in some NSTX-U scenarios. However, we do not consider those displacements here because they are expected to be nominally axisymmetric. Therefore they will not be resonant with the plasma, and will be automatically corrected by the plasma control system.

3. Analysis of the impact of error fields

Although the error field spectrum is not strongly dependent on the scenario, the plasma response to these error fields is strongly dependent. The differences in plasma response are due to the differing locations of the rational surfaces, and also to the relative proximity of the scenarios to marginal stability of kink modes and tearing modes [23]. In particular, the reduction of resonant fields in the linear plasma response, which corresponds to the screening of magnetic islands, is found to be very sensitive to the proximity of the plasma to tearing stability, which in turn is strongly dependent on the electron fluid rotation frequency [24]. For these cases we assume a model rotation profile in which the rotation is proportional to the square-root pressure, which is positive-definite and representative of the observed strong core rotation in NSTX-U.

3.1. Braking and locking

Resonant braking is caused by the interaction of response currents in the plasma with the perturbing magnetic field, and can lead to tearing mode instabilities through a reduction of rotation shear, or to error field penetration and mode locking. To estimate resonant braking and the tendency of the error field to cause locking, we consider the resonant $m/n = 2/1$ component of the total field and of the parallel current density at the $q = 2$ surface. These quantities are calculated using M3D-C1 [24], with a single-fluid resistive linear model, and independently with the ideal-MHD perturbed equilibrium code IPEC [20]. We note that in IPEC, the calculated resonant field is exactly zero, but an ‘effective’ total resonant field is inferred by considering what field would be present were the resonant currents to dissipate. In effect, the IPEC resonant field is a measure of the resonant parallel currents. An example of the effect of the plasma response is shown in figure 4, in which the total resonant field (symbols connected by solid lines) is compared to the resonant components of the error fields (dotted lines) in an NSTX-U discharge using the error fields calculated from the metrology results. It can be seen that the plasma response strongly reduces the total resonant fields, especially in the core where the plasma rotation is large.

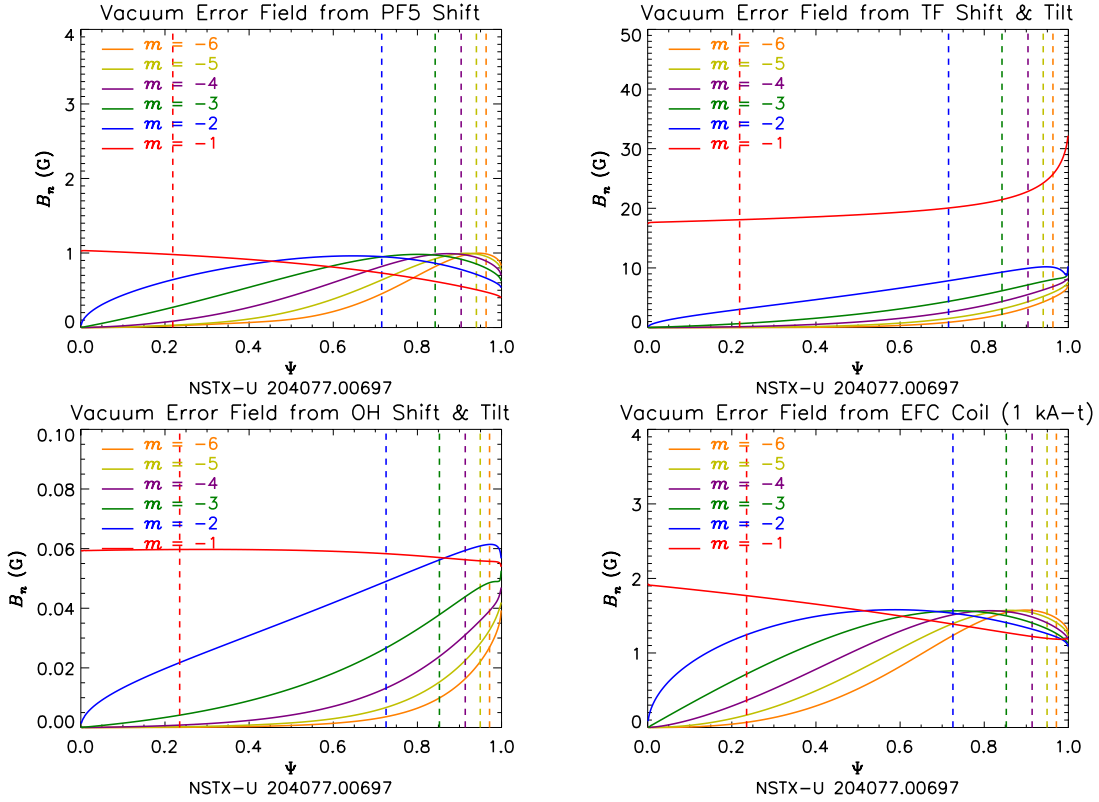


Figure 3. The $n = 1$, $-6 \leq m \leq -1$ spectral components of the error field, B_{mn} as defined in equation (3), versus the normalized poloidal flux Ψ due to the PF5, TF, OH, and EFC coils as calculated by M3D-C1 in NSTX-U discharge 204077 at $t = 697$. The vertical dashed lines indicate the locations of the respective mode-rational surfaces. For the PF5, TF, and OH coils, the fields are calculated using the measured misalignments and currents and the $n = 1$ displacements given in tables 1 and 2. For the EFC coil, the field is calculated assuming 1 kA-turn of current in an $n = 1$ configuration. Note that the vertical scales differ among the plots.

The 1/1 components, which we suspect may be playing an important role in NSTX-U, are not used here to estimate the impact on locking for two reasons. First, a correlation between the 1/1 component of the total resonant field and locking behavior has not yet been established quantitatively, and those studies that have considered the 1/1 component of the error field have found it to be subdominant to the 2/1 [25]. Second, equilibria containing a $q = 1$ surface are typically unstable to MHD modes, which contradicts the assumptions of the plasma response calculation that the response is small and time-independent, and which therefore raises questions about the validity of the calculated 1/1 component of the total resonant field. We also reiterate that it is the $q = 2$ surface that was routinely found to be locked in NSTX-U, though the 1/1 component could be playing an important role in that process by affecting the rotation profile globally.

We estimate the acceptable tolerances in coil alignment by calculating the largest magnitude of a shift or tilt of a coil that would result in an 2/1 field component less than or equal to the 2/1 component produced in response to the NSTX-U EFC coils powered at 1 kA-turn. Given the single-mode model, this is equivalent to the statement that the error field could be corrected by the EFC coils powered at 1 kA-turn, although this still may require a time-dependent EFC correction algorithm. This answer depends of course on the scenario, since the error

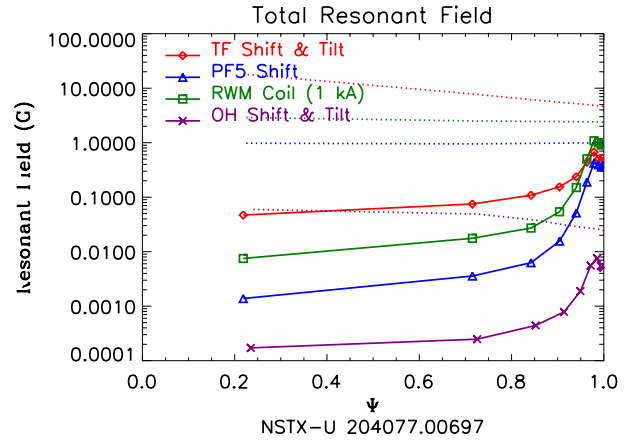


Figure 4. Results of plasma response calculations from M3D-C1 for NSTX-U discharge 204077 at $t = 697$ ms. Symbols connected by solid lines indicate the total resonant field from various error field sources. Dotted lines indicate the resonant fields from the applied field alone.

field from a coil depends on the current in the coil, and also because the parameters of the scenario (including shape and plasma β) affect the extent to which various coils couple to the plasma response. The answer also depends on the metric considered. Here, we consider the resonant component of the

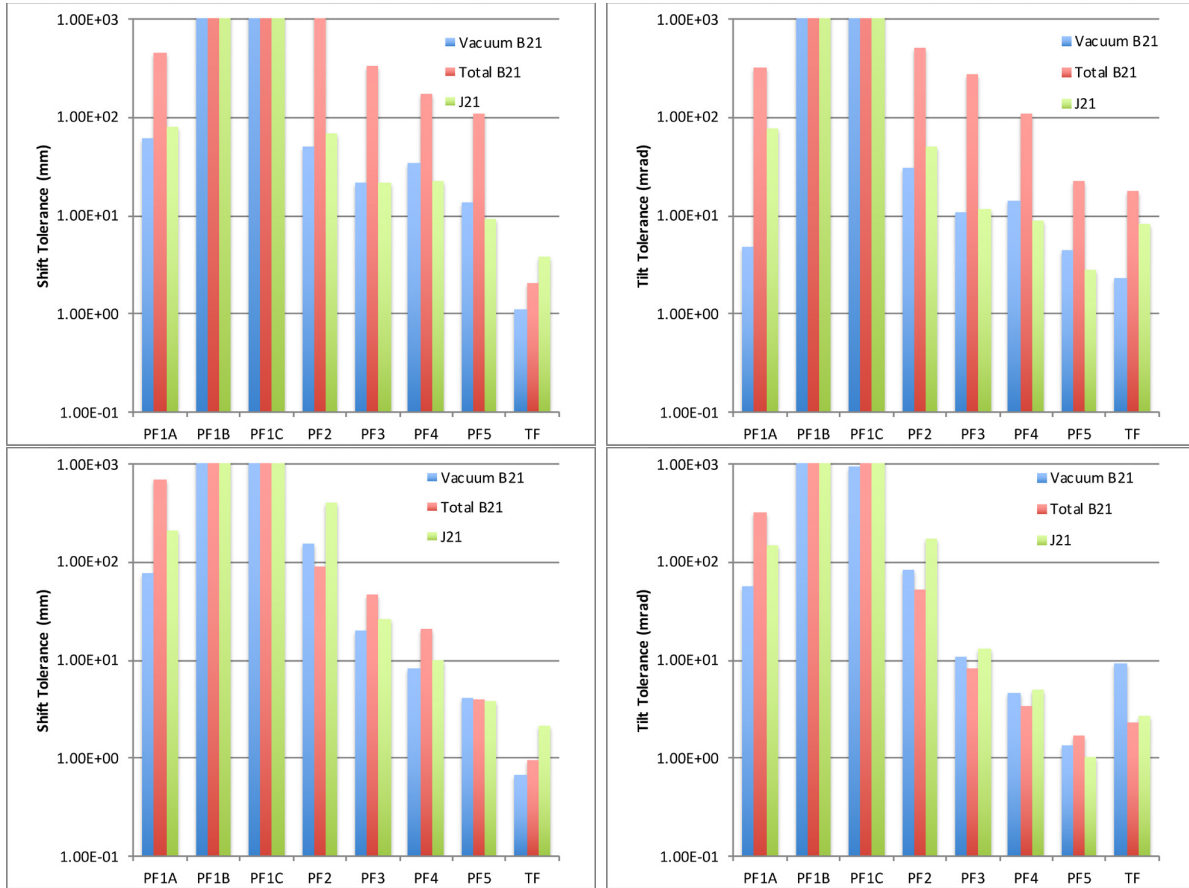


Figure 5. Estimated tolerances for coil shifts (left) and tilts (right) required for resonant field component to be correctable by the NSTX-U EFC coils powered at 1 kA-turn. These are based on M3D-C1 calculations using NSTX-U discharge 204077 at $t = 697$ ms (top) and the 2 MA model scenario 116313 (bottom), using the actual TF and PF coil currents for these scenarios (PF1B and PF4 are not used in these scenarios, so these coils are assigned the currents in PF1C and PF5, respectively, for estimating the tolerances).

Table 3. The maximum current allowed in each coil in NSTX-U [17, 26], and the maximum current allowed for 6 s equivalent square waveform (ESW) [26]. When calculating tolerances based on divertor heat flux considerations, the 6 s ESW currents are used.

Coil	PF1A	PF1B	PF1C	PF2	PF3	PF4	PF5	TF
Max. current (kA-t)	1171.2	416	318	420	480	544	1632	4700
6 s ESW current (kA-t)	698.22	163.3	156.51					

error field at the $q = 2$ surface ('Vacuum B_{21} '), the resonant component of the total field at the $q = 2$ surface ('Total B_{21} '), and the resonant component of the parallel current density at the $q = 2$ surface (' J_{21} '). The tolerances implied by these criteria for NSTX-U discharge 204077 at $t = 697$ ms and for the 2 MA model scenario 116313 are shown in figure 5. (The PF1B and PF4 coils are not used in these scenarios, so we assign to them the same currents as the PF1C and PF5 coils, respectively, for the purpose of calculating the tolerances.) Tolerances were also calculated assuming that the coils carried the maximum current needed for any scenario in the NSTX-U design basis [17]. These currents are listed in table 3, and the resulting tolerances are shown in figure 6.

Regardless of the chosen metric, it is found that the TF error field is generally the dominant source of resonant response from the plasma. This is true, despite the fact that the TF error

field spectrum is generally inefficient at driving resonant currents in the plasma, due to the large current in the TF rod and the proximity of the rod to the plasma. The plasma response to the TF error field is found to depend significantly on the presence of a $q = 1$ surface, since the TF error field is dominantly $m/n = 1/1$. This dependence can be seen in figure 7, which shows the total resonant field from IPEC calculations of the plasma response to the model TF and PF error fields in NSTX-U discharge 203077 at times before and after formation of the $q = 1$ surface. The dependence of the plasma response on the presence of the $q = 1$ surface is qualitatively consistent with results of several 'compass' scans performed during the NSTX-U run campaign, which found that the optimal error field correction before and after the formation of the $q = 1$ surface differed significantly. Interestingly, these discharges typically disrupted via locking of the $1/1$ surface, since the

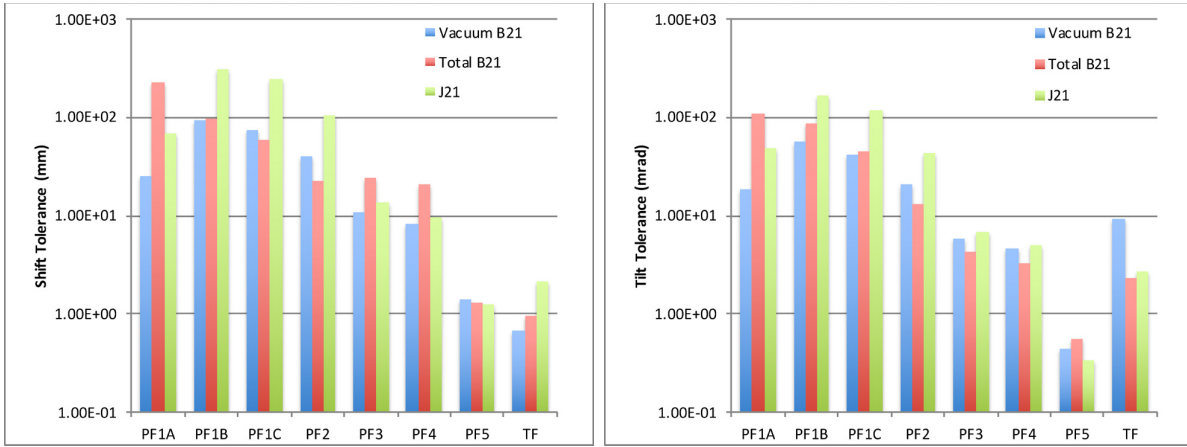


Figure 6. Estimated tolerances for coil shifts (left) and tilts (right) required for resonant field component to be correctable by the NSTX-U EFC coils powered at 1 kA-turn, if the PF and TF coils were using the maximum rated current. These are based on M3D-C1 calculations using 2 MA model scenario 116313.

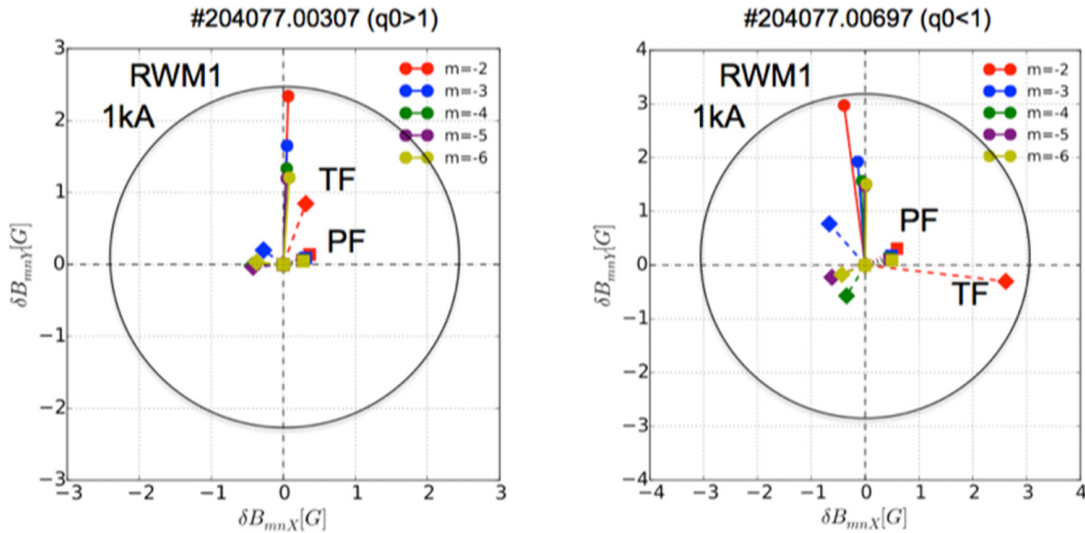


Figure 7. The magnitude and phase of various Fourier components of the total resonant field (applied field plus plasma response) arising from the calculated TF and PF error fields in NSTX-U, as calculated by IPEC. Values are shown for NSTX-U discharge 204077 at $t = 307$ (left) and $t = 697$ (right), which are before and after the formation of the $q = 1$ surface, respectively. The circle represents the total resonant field from the EFC coils powered at 1 kA.

$2/1$ surface was often locked *ab initio*. The $1/1$ component of the EFC coil spectrum is relatively weak, so this core locking phenomenon may be related to strong coupling between the $2/1$ and $1/1$ surfaces in ST geometry. The intrinsic error field may contribute to this coupling by limiting the differential rotation between the surfaces. In contrast, the PF1, PF2, and PF3 coils contribute relatively little to the resonant interaction, and tolerances for their alignment are correspondingly loose. (Of course, the $\gtrsim 1$ m tolerances calculated for the PF1s and PF2 coils should not be taken literally—the assumption of linearity we have made in these calculations will have been violated at displacements far smaller than this. These large values should simply be taken as an indication that other physics or engineering constraints will set the tolerances for these coils rather than error field considerations.)

Calculations of neoclassical toroidal viscosity have been carried out using GPEC [27] for a number of NSTX-U model scenarios. Generally, higher NTV is found at higher β_N due to the increase in plasma response as marginal kink stability is approached [23]. In a typical case, GPEC finds a total NTV torque on the order of 2 N m in a high-beta NSTX-U model equilibrium. This compares with neutral beam torque of 1–2 N m per source (depending on the particular source), and is therefore not negligible. Unlike resonant fields, the NTV is a radially distributed torque that is quadratic in δB , and therefore cannot be completely compensated by external coils, even in the ‘single-mode’ model. While NTV is an important consideration, setting coil tolerances based on NTV is challenging because the computed NTV torque strongly depends on the predicted rotation profile, which itself depends on

torques from error fields. Due to this uncertainty, we believe that NTV calculations should not drive engineering tolerances at this time.

Certain characteristics of the TF error field present new challenges for error field correction. Specifically, the error field spectrum differs significantly from that of coils on the low-field side (such as the NSTX-U EFC coils), and does not resonate strongly with the dominant kink mode, thus potentially requiring multi-mode correction. Furthermore, IPEC calculations agree with experimental results in finding that the optimal correction phase and amplitude changes as the plasma current density profile evolves, although the predicted correction phase disagrees with the empirical optimal phase after the formation of the $q = 1$ surface, possibly due to the fact that a $2/1$ island is already present in contravention of the assumption of linearity. This change in phase suggests that while EFC with the existing EFC coils may be possible, it would likely require a time-dependent correction algorithm that will be sensitive to plasma parameters (e.g. current density profile), and that is not easily predictable with present tools. This could pose a significant challenge to reliable high-performance operation of NSTX-U if the TF error is not reduced.

3.2. Divertor heat flux

Substantial heat loads on plasma facing components (PFCs) are predicted for high-performance NSTX-U scenarios. Mitigating surface heat flux through poloidal flux expansion may require $B_p/B_T < 0.02$. Error fields will lead to a toroidal variation in this pitch angle, and may therefore lead to toroidally localized regions of increased heat flux. Additionally, the formation of lobes due to the deformation of the topologically unstable x -point region in diverted plasmas can lead to an expansion of the wetted area of the divertor PFCs. This can have the beneficial effect of spreading the heat flux over a larger area, but it can also be problematic if it leads to toroidal localization of heat flux deposition or the deposition of heat outside of the intended target region.

To assess the impact of error fields on the magnetic footprint and pitch angle at the divertor plates, we have used the model NSTX-U equilibrium based on NSTX H-mode discharge 116313, with profiles scaled such that $I_p = 2$ MA and $B_T = 1$ T. Perturbed equilibria were calculated with M3D-C1, and the perturbation to the pitch angle was measured along the vertical and horizontal divertor plates (roughly $R = 0.45$ m and $Z = -1.6$ m, respectively). It is found that the maximum perturbation to the pitch angle due to the error field alone (in the absence of plasma response) on the vertical and horizontal plates is roughly 7.5 mrad (0.43°) and 1.5 mrad (0.09°), respectively. The plasma response is generally found to increase the maximum perturbation to the pitch angle, especially at the horizontal target.

We calculate tolerances for the shift and tilt of individual coils by constraining the fractional perturbation to the magnetic pitch angle at the divertor to be less than 10%. The resulting tolerances are shown in figure 8, where we have used the 2 MA model scenario 116313 (the L-mode discharge is

not considered here because heat fluxes will not be problematic in that case). When calculating these tolerances, we have considered both the actual coil currents in the scenario and the maximum rated currents. In the latter case we have used the current allowed for an equivalent square-wave time of 6 s for the PF1 coils. This is because the worst-case scenario for heat fluxes is in the 2 MA, 5 s scenario for which the I_p waveform has an equivalent square wave time of 6 s. These currents are shown in table 3. For these tolerances, the alignment in question is that between the coil and the plasma facing surfaces, whereas the tolerances set by the resonant fields refer to the relative orientations of the various magnets.

Again, it is found the most stringent tolerances are generally on the TF center rod alignment. Unlike for resonant fields, however, the tolerances set by the pitch angle constraint is more severe for the PF1s and PF2 than for the PF3–5 coils. Also unlike the result for the resonant field, the plasma response has a relatively weak influence on these tolerances. This is because the response currents inside the plasma are not strongly driven by the PF1s and PF2, and are relatively far from the divertor plates.

The divertor footprint was calculated using TRIP3D, taking the magnetic field from the M3D-C1 perturbed equilibrium calculations. An example of the perturbed field orbits and footprints on the lower horizontal divertor from TF and PF5L error fields are shown in figure 9. The colours in this figure indicate the radial depth to which a field line penetrates, and is used here as a rough proxy for the temperature of the field line, and the coloured area indicates the expected wetted area of the divertor plate. For a given perturbation spectrum, we find that the linear extent of the footprint on the divertor scales approximately linearly with the perturbation amplitude. Thus, to the extent that the plasma response remains linear in the error field strength, the footprint extent will approximately depend linearly on the shift, tilt, and current in a coil. More extensive calculations and analysis of the divertor footprints are being prepared as part of a separate publication [28].

3.3. Challenges to calculating response to shifted coils

It is clear that the plasma response to the TF shifting in one direction should be equivalent to shifting all of the PF coils in the opposite direction, up to a shift in coordinates. Due to the differing coordinates, $\delta\vec{B}$ will *not* be equivalent in the two cases. However, coordinate-independent measures of the plasma response, such as magnetic island widths and resonant field components, should be equivalent. Indeed, as noted in section A.3, the difference in coordinate systems is equivalent to an ideal-MHD plasma response with displacement $\vec{\xi}_\delta = \delta e^{i(\varphi - \varphi_s)} (\hat{R} + i\hat{\varphi})$, and therefore it does not affect the resonant components of the magnetic field (this is proved in appendix B).

Thus, a numerical code must be able to represent the solution $\delta\vec{B} = \nabla \times (\vec{\xi}_\delta \times \vec{B}_0)$ in order to correctly predict the equivalence of the coordinate-independent properties of the plasma response in the two cases. In fact, as presently constituted, there remain questions about whether either IPEC

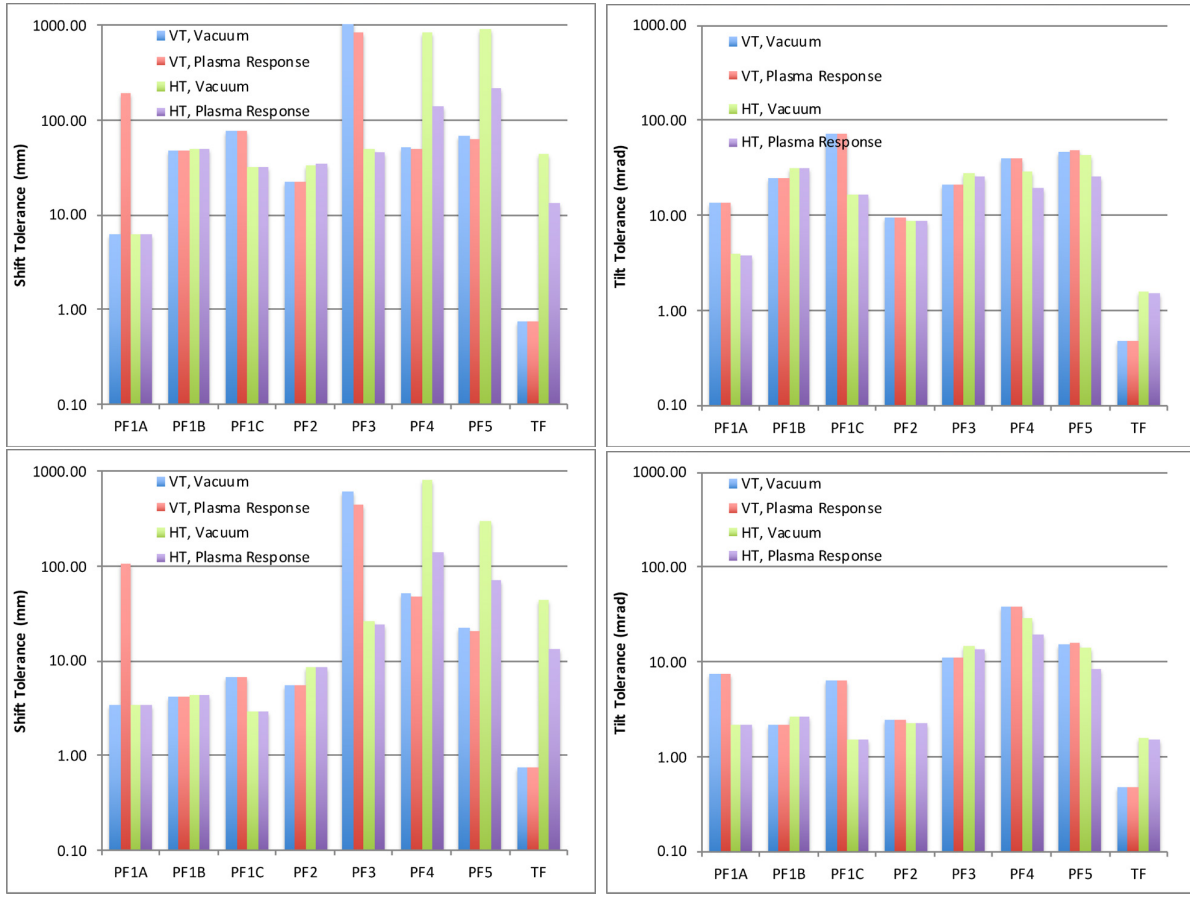


Figure 8. The shift (left) or tilt (right) of each coil that results in a 10% fractional change to the magnetic pitch angle on the horizontal divertor target (HT) or vertical divertor target (VT), using 2 MA NSTX-U model scenario 116313. Tolerances are calculated for both the actual coil currents in this scenario (top) and for the maximum allowed coil currents (bottom).

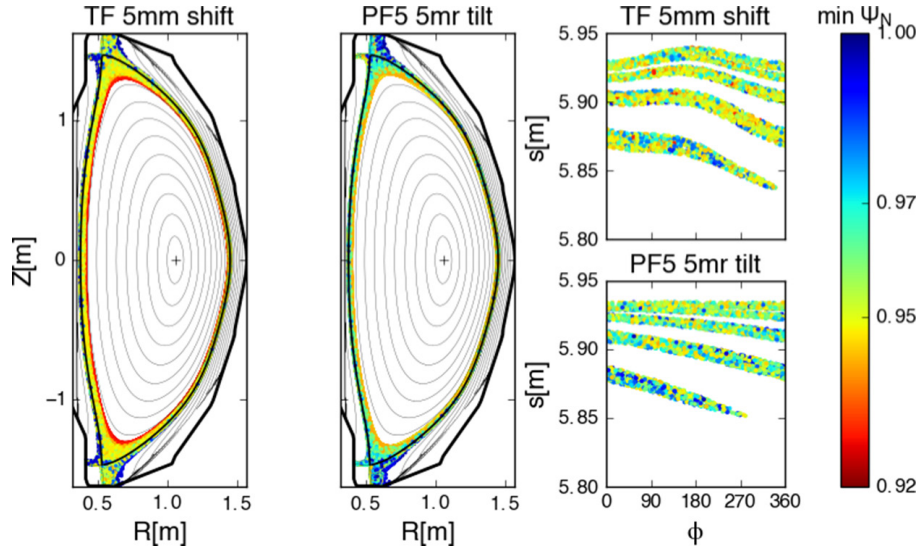


Figure 9. Poincaré plots (left) and lower horizontal divertor footprints (right) of the magnetic field lines that hit the wall due to a 5 mm shift of the TF center rod and a 5 mrad tilt of the PF5L coil. The colours represent the minimum normalized poloidal flux Ψ_N reached by each field line, which serves as a proxy for the field line temperature.

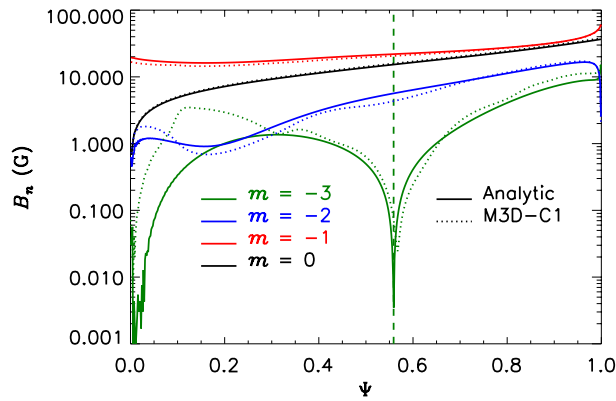


Figure 10. *Solid lines:* an analytic calculation of the spectral components of $\delta\vec{B}$ resulting from a horizontal shift of the coordinate system by -5 mm for an axisymmetric NSTX-U model equilibrium. *Dotted lines:* an M3D-C1 calculation of $\delta\vec{B}$ for a perturbed plasma equilibrium given error fields corresponding to a horizontal shift of all coils by a distance 5 mm. The vertical dashed line is the $q = 3$ surface (this model equilibrium does not have a $q = 2$ surface).

or M3D-C1 can exactly represent this solution. In the case of IPEC, this solution is excluded by the boundary condition $\vec{\zeta} = 0$ at the magnetic axis, which has been used in the calculations presented in this paper. In the case of M3D-C1, the boundary condition that the component of $\delta\vec{B}$ normal to the computational domain boundary (which can be far from the plasma) is due entirely to the field from the coils may also exclude the correct solution, because in the correct solution part of $\delta\vec{B}$ on the boundary is due to the shift of the plasma current.

To test how accurately M3D-C1 is able to represent this solution, we ran a calculation in which all coils were shifted by 5 mm in the same direction. We expect the plasma response to be a rigid shift by 5 mm in the same direction, so that the final field distribution is exactly the same as the initial equilibrium (without shifted coils), but shifted by -5 mm. This is equivalent to a coordinate shift in the opposite direction, and therefore should yield the ‘response’ $\delta\vec{B} = \nabla \times (\vec{\zeta}_\delta \times \vec{B}_0)$ exactly, which can easily be calculated from the equilibrium magnetic field \vec{B}_0 . We compare this analytically computed field with that calculated by M3D-C1 in figure 10. The agreement is generally good, but whereas the resonant components of the perturbed field vanish exactly at the mode-rational surfaces in the analytic result, core resonant fields on the order of 0.1 G are present in the M3D-C1 result. While small relative to the non-resonant magnitudes, which exceed 30 G in some places, it is non-negligible compared to typical tokamak error fields, for which the vacuum resonant fields themselves are of order 1 G, and the total resonant fields including plasma response are often smaller by an order of magnitude or more due to screening. Thus, even small relative errors in representing the shifted solution can lead to large errors in the total resonant field, due to the large magnitude of $\delta\vec{B}$ implied by the coordinate transformation.

These issues are less important for the calculations of the perturbed footprints and pitch angles on the divertor plates. These effects are not coordinate invariant, since the coordinate

system is defined by the positions of the divertor plates. Furthermore, these effects are strongly influenced by the non-resonant components of the field, which are less sensitive than the resonant components on a fractional basis.

4. Summary

Experiments, metrology, and perturbed equilibrium modeling all suggest that the dominant source of field error in the 2016 NSTX-U configuration was likely from the misalignment of the TF rod. This field error is dominantly $|m| = n = 1$, is expected to couple strongly to the plasma through resonant interaction (i.e. excitation of kink modes) primarily in the presence of a $q = 1$ surface. Plasma response calculations from both codes suggest that the resonant currents elicited by the TF error field are comparable to those elicited by the EFC coils powered at 1 kA-turn, despite the significantly larger vacuum fields from the TF error. Error fields from eddy currents in the vacuum vessel and passive plates during IP ramp-up were also calculated using VALEN [29]. The resonant error fields from these currents were found to be below 1 G, and are therefore not presently considered to be a likely source of the observed error fields. The PF5 error field, while significant, is also expected to be more easily corrected by the NSTX-U EFC coils than the TF error field, especially when multiple response modes are important, due to the spectral similarity between the PF5 error field and EFC coil field. Calculations of total resonant fields due to possible misalignments of other poloidal field coils generally find a weaker response per mm-Amp-turn or mrad-Amp-turn, especially for the coils in the divertor region (the PF1s and PF2). Changing the alignment of these coils within mechanical tolerances is not expected to have any appreciable effect on resonant braking or mode locking, with the exception of the PF4 coils, which are found to couple to the plasma response nearly as well as the PF5.

Tolerances on coil alignments were calculated based on two constraints: first, that the 2/1 resonant error field remained smaller than the resonant field from the EFC coils powered at 1 kA-turn; and second, that the fractional perturbation to the magnetic field pitch at the divertor plates remained less than 10%. The alignment tolerances of the PF4 and PF5 coils are found to be set by the first constraint, and the tolerances of the PF1s and PF2 are found to be set by the second. Both constraints lead to relatively tight (~ 1 mm and ~ 1 mrad) tolerances for the TF alignment, both relative to the other magnetic coils, and relative to the plasma facing components of the divertor.

We believe the tolerances obtained here represent conservative estimates, for several reasons. First, the requirements that the resonant field be correctable by only 1 kA-turn of current in the EFC coils (which have a maximum current of 6.6 kA-turns [30]) and that the fractional variation in the pitch angle is less than 10% are relatively conservative. Second, it is plausible that a spuriously resonant field is being calculated for the TF tilt and shift for the reasons outlined in section 3.3. Finally, although edge locking was observed in the low-density L-modes that were frequently run in the 2016 NSTX-U

campaign, this locking was not observed to cause disruptions. The locked edge was also observed to unlock upon entering H-mode, when density increased. Therefore we have confidence that stable, high-performance plasmas can be run even with the coil alignments outside of the tolerances described here, as they were during the 2016 campaign. Still, this analysis gives a useful indication of the relative impact of locking and heat flux considerations on coil tolerances, and of the relative effect of misalignments of the various coils.

These results, together with calculations for other NSTX-U equilibria and model scenarios, have been used to drive new engineering tolerance requirements for NSTX-U as it is rebuilt. A trial fit-up of the TF center rod has found that it can be aligned to the CS casing to within 0.4 mm and 0.14 mrad. This should alleviate the most serious concerns about toroidally localized heating of the inner vessel plasma facing components, which are aligned to the CS casing. This should also simplify the reduction of magnetic braking and locking by providing a clear reference frame for aligning the vertical field coils. If this alignment can be made successfully, we expect a dramatic reduction in electromagnetic torque and an expansion of accessible parameter space, particularly with regard to density and collisionality, when NSTX-U resumes operation.

Acknowledgments

We thank J. Bialek for a VALEN calculation of the vessel currents during an NSTX-U current ramp and M. Mardenfeld for metrology data and useful discussion regarding the interface between physics and engineering uncertainty. This work was supported by the United States Department of Energy under contracts DE-AC02-09CH11466, DE-AC05-00OR22725, DE-SC0012706, and DE-FC02-04ER54698.

Appendix A. Shift-tilt coordinate transformation

In this section, we describe in detail the transformation of the magnetic field components from a coordinate system $\vec{r} = (r, \phi, z)$ in which the field components are known to a new coordinate system $\vec{R} = (R, \varphi, Z)$ that is shifted and tilted with respect to \vec{r} . The difference between the field in the ‘lab’ coordinates and the field in the ‘coil’ coordinates, $\delta\mathbf{B}(\vec{R}) = \vec{B}(\vec{R}) - \vec{B}(\vec{r})$, is equivalent to the error field due to a shift and tilt of the coil. The generic transformation is considered first, and this is then specialized to the case where the shift and tilt are small, and the coils are axisymmetric in \vec{r} . In this limit, our results are consistent with a previous analysis of the error field from the shift and tilt of poloidal field coils by La Haye and Scoville [18].

A.1. General transformation

Let \vec{R} be shifted with respect to \vec{r} by δ in the direction $\varphi = \varphi_s$, and a tilted by angle α along the axis $\varphi = \varphi_t$. It is most convenient to calculate the coordinate transformation from \vec{r} to \vec{R} by using Cartesian coordinates, where

$$x = r \cos(\phi) \quad y = r \sin(\phi)$$

$$X = R \cos(\varphi) \quad Y = R \sin(\varphi).$$

We can express the Cartesian coordinate transformations using a series of rotations and a translation:

$$\vec{x} = R_x(-\varphi_t) \cdot R_y(\alpha) \cdot R_x(\varphi_t - \varphi_s) \cdot [T_x(-\delta) + R_x(\varphi_s) \cdot \vec{X}] \quad (\text{A.1})$$

where

$$\vec{x} = \begin{pmatrix} x \\ y \\ z \end{pmatrix} \quad \vec{X} = \begin{pmatrix} X \\ Y \\ Z \end{pmatrix}$$

$$R_x(u) = \begin{pmatrix} \cos u & \sin u & 0 \\ -\sin u & \cos u & 0 \\ 0 & 0 & 1 \end{pmatrix}$$

$$R_y(u) = \begin{pmatrix} 1 & 0 & 0 \\ 0 & \cos u & \sin u \\ 0 & -\sin u & \cos u \end{pmatrix}$$

$$T_x(u) = (u \ 0 \ 0).$$

The final rotation ($R_x(-\varphi_t)$) in equation (A.1) is done to ensure that $\phi = \varphi$ in the limit that α and δ vanish. This results in the following relation between the Cartesian components of the coil coordinates and those of the lab coordinates:

$$\vec{x} = M \cdot \vec{X} + \vec{b} \quad (\text{A.2})$$

where

$$M = \begin{pmatrix} \cos^2 \frac{\alpha}{2} + \cos(2\varphi_t) \sin^2 \frac{\alpha}{2} & (1 - \cos \alpha) \cos \varphi_t \sin \varphi_t & -\sin \alpha \sin \varphi_t \\ (1 - \cos \alpha) \cos \varphi_t \sin \varphi_t & \cos^2 \frac{\alpha}{2} - \cos(2\varphi_t) \sin^2 \frac{\alpha}{2} & \sin \alpha \cos \varphi_t \\ \sin \alpha \sin \varphi_t & -\sin \alpha \cos \varphi_t & \cos \alpha \end{pmatrix}$$

$$\vec{b} = \delta \begin{pmatrix} -\cos^2 \frac{\alpha}{2} \cos \varphi_s - \sin^2 \frac{\alpha}{2} \cos(\varphi_s - 2\varphi_t) \\ -\cos^2 \frac{\alpha}{2} \sin \varphi_s + \sin^2 \frac{\alpha}{2} \sin(\varphi_s - 2\varphi_t) \\ \sin \alpha \sin(\varphi_s - \varphi_t) \end{pmatrix}.$$

Noting that

$$\begin{pmatrix} \hat{r} \\ \hat{\phi} \\ \hat{z} \end{pmatrix} = R_x(\phi) \begin{pmatrix} \hat{x} \\ \hat{y} \\ \hat{z} \end{pmatrix} \quad (\text{A.3})$$

we obtain an expression relating the unit vectors in the coil coordinates to those in the lab coordinates:

$$\begin{pmatrix} \hat{r} \\ \hat{\phi} \\ \hat{z} \end{pmatrix} = R_x(\phi) \cdot M \cdot R_x(-\varphi) \cdot \begin{pmatrix} \hat{R} \\ \hat{\varphi} \\ \hat{Z} \end{pmatrix} \quad (\text{A.4})$$

$$= D \cdot \begin{pmatrix} \hat{R} \\ \hat{\varphi} \\ \hat{Z} \end{pmatrix} \quad (\text{A.5})$$

where

$$\begin{aligned}
D_{\hat{r}\hat{R}} &= \cos^2 \frac{\alpha}{2} \cos(\phi - \varphi) + \sin^2 \frac{\alpha}{2} \cos(\phi + \varphi - 2\varphi_t) \\
D_{\hat{r}\hat{\varphi}} &= \cos^2 \frac{\alpha}{2} \sin(\phi - \varphi) - \sin^2 \frac{\alpha}{2} \sin(\phi + \varphi - 2\varphi_t) \\
D_{\hat{r}\hat{z}} &= \sin \alpha \sin(\phi - \varphi_t) \\
D_{\hat{\phi}\hat{R}} &= -\cos^2 \frac{\alpha}{2} \sin(\phi - \varphi) - \sin^2 \frac{\alpha}{2} \sin(\phi + \varphi - 2\varphi_t) \\
D_{\hat{\phi}\hat{\varphi}} &= \cos^2 \frac{\alpha}{2} \cos(\phi - \varphi) - \sin^2 \frac{\alpha}{2} \cos(\phi + \varphi - 2\varphi_t) \\
D_{\hat{\phi}\hat{z}} &= \sin \alpha \cos(\phi - \varphi_t) \\
D_{\hat{z}\hat{R}} &= -\sin \alpha \sin(\varphi - \varphi_t) \\
D_{\hat{z}\hat{\varphi}} &= -\sin \alpha \cos(\varphi - \varphi_t) \\
D_{\hat{z}\hat{z}} &= \cos \alpha.
\end{aligned} \tag{A.6}$$

Given the magnetic field in the coil coordinates (r, ϕ, z) , we may evaluate the field in the lab coordinates (R, φ, Z) by expanding (r, ϕ, z) in terms of (R, φ, Z) using equation (A.2) together with the standard definitions of cylindrical coordinates; and by expanding \hat{r} , $\hat{\phi}$, and \hat{z} in terms of \hat{R} , $\hat{\varphi}$, and \hat{Z} using equation (A.5).

A.2. Linear transformation

In the limit where $\alpha \ll 1$ and $\delta \ll R$, the coil coordinates \vec{r} are approximately related to the lab coordinates \vec{R} by linear functions of δ and α . We find

$$\frac{\partial}{\partial \delta} \begin{pmatrix} r \\ \phi \\ z \end{pmatrix} = \begin{pmatrix} -\cos(\varphi - \varphi_s) \\ \frac{1}{R} \sin(\varphi - \varphi_s) \\ 0 \end{pmatrix} \tag{A.7}$$

$$\frac{\partial}{\partial \alpha} \begin{pmatrix} r \\ \phi \\ z \end{pmatrix} = \begin{pmatrix} Z \sin(\varphi - \varphi_t) \\ \frac{Z}{R} \cos(\varphi - \varphi_t) \\ -R \sin(\varphi - \varphi_t) \end{pmatrix} \tag{A.8}$$

and therefore, noting that $\vec{r} = \vec{R}$ in the limit that $\delta \rightarrow 0$ and $\alpha \rightarrow 0$,

$$r \approx R - \delta \cos(\varphi - \varphi_s) + Z\alpha \sin(\varphi - \varphi_t) \tag{A.9}$$

$$\phi \approx \varphi - \frac{\delta}{R} \sin(\varphi - \varphi_s) + \frac{Z\alpha}{R} \cos(\varphi - \varphi_t) \tag{A.10}$$

$$z \approx Z - R\alpha \sin(\varphi - \varphi_t) \tag{A.11}$$

$$\frac{\partial}{\partial \delta} \begin{pmatrix} \hat{r} \\ \hat{\phi} \\ \hat{z} \end{pmatrix} = \begin{pmatrix} 0 & \frac{1}{R} \sin(\varphi - \varphi_s) & 0 \\ -\frac{1}{R} \sin(\varphi - \varphi_s) & 0 & 0 \\ 0 & 0 & 0 \end{pmatrix} \begin{pmatrix} \hat{R} \\ \hat{\varphi} \\ \hat{Z} \end{pmatrix} \tag{A.12}$$

$$\frac{\partial}{\partial \alpha} \begin{pmatrix} \hat{r} \\ \hat{\phi} \\ \hat{z} \end{pmatrix} = \begin{pmatrix} 0 & \frac{Z}{R} \cos(\varphi - \varphi_t) & \sin(\varphi - \varphi_t) \\ -\frac{Z}{R} \cos(\varphi - \varphi_t) & 0 & \cos(\varphi - \varphi_t) \\ -\sin(\varphi - \varphi_t) & -\cos(\varphi - \varphi_t) & 0 \end{pmatrix} \begin{pmatrix} \hat{R} \\ \hat{\varphi} \\ \hat{Z} \end{pmatrix} \tag{A.13}$$

$$\begin{pmatrix} \hat{r} \\ \hat{\phi} \\ \hat{z} \end{pmatrix} \approx \begin{pmatrix} 1 & \frac{\delta}{R} \sin(\varphi - \varphi_s) + \frac{Z\alpha}{R} \cos(\varphi - \varphi_t) & \alpha \sin(\varphi - \varphi_t) \\ -\frac{\delta}{R} \sin(\varphi - \varphi_s) - \frac{Z\alpha}{R} \cos(\varphi - \varphi_t) & 1 & \alpha \cos(\varphi - \varphi_t) \\ -\alpha \sin(\varphi - \varphi_t) & -\alpha \cos(\varphi - \varphi_t) & 1 \end{pmatrix} \begin{pmatrix} \hat{R} \\ \hat{\varphi} \\ \hat{Z} \end{pmatrix}. \tag{A.14}$$

We may Taylor expand \vec{B} in α and δ , noting that $\vec{r}(\delta = 0, \alpha = 0) = \vec{R}$:

$$\vec{B}(\vec{R}) \approx \vec{B}(\vec{r}) + \delta \partial_\delta \vec{B}(\vec{R}) + \alpha \partial_\alpha \vec{B}(\vec{R}) \quad (\text{A.15})$$

where (here and henceforth all quantities are evaluated at \vec{R}):

$$\begin{aligned} \partial_\delta \vec{B} &= B_r \partial_\delta \hat{r} + B_\phi \partial_\delta \hat{r} + B_z \partial_\delta \hat{z} \\ &+ [\partial_r B_r \partial_\delta r + \partial_\phi B_r \partial_\delta \phi + \partial_z B_r \partial_\delta z] \hat{r} \\ &+ [\partial_r B_\phi \partial_\delta r + \partial_\phi B_\phi \partial_\delta \phi + \partial_z B_\phi \partial_\delta z] \hat{\phi} \\ &+ [\partial_r B_z \partial_\delta r + \partial_\phi B_z \partial_\delta \phi + \partial_z B_z \partial_\delta z] \hat{z}. \end{aligned} \quad (\text{A.16})$$

Thus, the linear transformation is

$$\begin{aligned} \vec{B}(\vec{R}) &= \vec{B}(\vec{r}) + \delta \left[-\partial_r B_r \cos(\varphi - \varphi_s) + \frac{1}{R} (\partial_\phi B_r - B_\phi) \sin(\varphi - \varphi_s) \right] \hat{R} \\ &+ \delta \left[-\partial_r B_\phi \cos(\varphi - \varphi_s) + \frac{1}{R} (\partial_\phi B_\phi + B_r) \sin(\varphi - \varphi_s) \right] \hat{\phi} \\ &+ \delta \left[-\partial_r B_z \cos(\varphi - \varphi_s) + \frac{1}{R} \partial_\phi B_z \sin(\varphi - \varphi_s) \right] \hat{Z} \\ &+ \alpha \left[\frac{Z}{R} (\partial_\phi B_\phi - B_\phi) \cos(\varphi - \varphi_t) + (Z \partial_r B_r - R \partial_z B_z) \sin(\varphi - \varphi_t) \right] \hat{R} \\ &+ \alpha \left[\left(\frac{Z}{R} (B_r + \partial_\phi B_\phi) - B_z \right) \cos(\varphi - \varphi_t) + R \partial_z B_\phi \sin(\varphi - \varphi_t) \right] \hat{\phi} \\ &+ \alpha \left[\left(B_\phi + \frac{Z}{R} \partial_\phi B_z \right) \cos(\varphi - \varphi_t) + (B_r + Z \partial_r B_z - R \partial_z B_z) \sin(\varphi - \varphi_t) \right] \hat{Z}. \end{aligned} \quad (\text{A.17})$$

Note that the ‘perturbed’ field, $\delta \vec{B}(\vec{R}) = \vec{B}(\vec{R}) - \vec{B}(\vec{r})$ is equivalent to that obtained through the ideal-MHD displacement

$$\begin{aligned} \vec{\xi} &= \delta \left[\cos(\varphi - \varphi_s) \hat{R} - \sin(\varphi - \varphi_s) \hat{\phi} \right] \\ &+ \alpha \left[-Z \sin(\varphi - \varphi_t) \hat{R} - Z \cos(\varphi - \varphi_t) \hat{\phi} + R \sin(\varphi - \varphi_t) \hat{Z} \right] \end{aligned} \quad (\text{A.18})$$

where the perturbed field is

$$\delta \vec{B} = \nabla \times \left[\vec{\xi} \times \vec{B}(\vec{r}) \right].$$

A.3. Axisymmetric fields

For fields that are axisymmetric in the coordinate system of the coil, $\partial_\phi \rightarrow 0$. In this case, the toroidal dependence of the field in the shifted / tilted coordinate system is entirely due to the shift and tilt. To first order in δ and α , this perturbation has toroidal mode number $n = 1$; i.e.

$$\vec{B} = \vec{B}_0 + \Re \left[(\vec{B}_\delta + \vec{B}_\alpha) e^{i\varphi} \right]. \quad (\text{A.19})$$

If \vec{B}_δ is known, the real and imaginary parts of \vec{B}_δ can be determined simply by evaluating \vec{B}_δ at $\varphi = 0$ and $\varphi = -\pi/2$, respectively.

$$\cos(\varphi - \beta) \rightarrow \cos(-\beta) + i \cos(-\pi/2 - \beta) = e^{-i\beta} \quad (\text{A.20})$$

$$\sin(\varphi - \beta) \rightarrow \sin(-\beta) + i \sin(-\pi/2 - \beta) = -ie^{-i\beta}. \quad (\text{A.21})$$

Therefore, we can write the linear transformation, equation (A.17), of axisymmetric fields, in complex notation as

$$\begin{aligned} \vec{B}(\vec{R}) &= \vec{B}(\vec{r}) + \delta e^{-i\varphi_s} \left\{ \begin{array}{l} [-\partial_r B_r + i \frac{1}{R} B_\phi] \hat{R} \\ - [i \frac{1}{R} B_r + \partial_r B_\phi] \hat{\phi} \\ - \partial_r B_z \hat{Z} \end{array} \right\} \\ &+ \alpha e^{-i\varphi_t} \left\{ \begin{array}{l} [i(R \partial_z B_r - Z \partial_r B_r) - \frac{Z}{R} B_\phi + i B_z] \hat{R} \\ + [\frac{Z}{R} B_r + i(R \partial_z B_\phi - Z \partial_r B_\phi) - B_z] \hat{\phi} \\ + [-i B_r + B_\phi + i(R \partial_z B_z - Z \partial_r B_z)] \hat{Z} \end{array} \right\}. \end{aligned} \quad (\text{A.22})$$

We note here that the perturbed field $\delta\vec{B} = \vec{B}(\vec{R}) - \vec{B}(\vec{r})$ can be written as the an ideal MHD displacement

$$\vec{\xi} = \delta e^{i\varphi - \varphi_s} (\hat{R} + i\hat{Z}) + \alpha e^{i\varphi - \varphi_s} (iZ\hat{R} - Z\hat{\varphi} - iR\hat{Z}).$$

A.3.1. Toroidal field coils. Toroidal field coils produce the magnetic field

$$\vec{B}^{\text{TF}} = \frac{\mu_0 I}{2\pi r} \hat{\phi}. \quad (\text{A.23})$$

Transforming this into (R, φ, Z) coordinates yields

$$\vec{B}^{\text{TF}}(R, Z) = \frac{\mu_0 I}{2\pi R} \hat{\phi} + \frac{\mu_0 I}{2\pi R} \left\{ \begin{array}{l} [i\frac{\delta}{R}e^{-i\varphi_s} - \alpha\frac{Z}{R}e^{-i\varphi_s}] \hat{R} \\ + [\frac{\delta}{R}e^{-i\varphi_s} + i\alpha\frac{Z}{R}e^{-i\varphi_s}] \hat{\varphi} \\ + \alpha e^{-i\varphi_s} \hat{Z} \end{array} \right\}. \quad (\text{A.24})$$

A.3.2. Poloidal field coils. Specializing to the case of poloidal field coils, for which $B_\phi = 0$, the transformation becomes

$$\vec{B}(R, Z) = \vec{B}(r, z) + \delta e^{-i\varphi_s} \left[-\partial_r B_r \hat{R} - i\frac{1}{R} B_r \hat{\varphi} - \partial_r B_z \hat{Z} \right] + \alpha e^{-i\varphi_s} \left\{ \begin{array}{l} i(B_z + R\partial_z B_r - Z\partial_r B_r) \hat{R} \\ + (\frac{Z}{R} B_r - B_z) \hat{\varphi} \\ i(-B_r + R\partial_z B_z - Z\partial_r B_z) \hat{Z} \end{array} \right\}. \quad (\text{A.25})$$

Appendix B. Proof that resonant field components vanish under ideal displacement

For any perturbation of the form $\delta B = \nabla \times (\vec{\xi} \times \vec{B})$,

$$\begin{aligned} \delta\vec{B} \cdot \nabla\psi e^{im\theta - in\varphi} &= \nabla \times (\vec{\xi} \times \vec{B}) \cdot \nabla\psi e^{im\theta - in\varphi} \\ &= \vec{B} \cdot \nabla(\vec{\xi} \cdot \nabla\psi) e^{im\theta - in\varphi} \\ &= \vec{B} \cdot \nabla(\vec{\xi} \cdot \nabla\psi e^{im\theta - in\varphi}) - i\vec{\xi} \\ &\quad \cdot \nabla\psi \vec{B} \cdot \nabla\theta (m - nq) e^{im\theta - in\varphi}. \end{aligned}$$

Here we have used the fact that $\vec{B} \cdot \nabla\varphi = q\vec{B} \cdot \nabla\theta$ in a straight field-line coordinate system. Inserting this expression into equation (3), the first term will vanish, leaving only the term proportional to $(m - nq)$ in the integrand. Thus, the resonant components of δB_{mn} (i.e. those for which $m = nq$) must vanish.

ORCID iDs

N.M. Ferraro  <https://orcid.org/0000-0002-6348-7827>
 J.-K. Park  <https://orcid.org/0000-0003-2419-8667>
 C.E. Myers  <https://orcid.org/0000-0003-4539-8406>
 S.P. Gerhardt  <https://orcid.org/0000-0002-2546-2194>
 J.E. Menard  <https://orcid.org/0000-0003-1292-3286>
 S. Munaretto  <https://orcid.org/0000-0003-1465-0971>
 M.L. Reinke  <https://orcid.org/0000-0003-4413-9613>

References

- [1] Nave M.F.F. and Wesson J.A. 1990 Mode locking in tokamaks *Nucl. Fusion* **30** 2575
- [2] Fitzpatrick R. 1993 Interaction of tearing modes with external structures in cylindrical geometry *Nucl. Fusion* **33** 1049
- [3] Shaing K.C. 2003 Magnetohydrodynamic-activity-induced toroidal momentum dissipation in collisionless regimes in tokamaks *Phys. Plasmas* **10** 1443
- [4] Cole A.J., Hegna C.C. and Callen J.D. 2008 Neoclassical toroidal viscosity and error-field penetration in tokamaks *Phys. Plasmas* **15** 056102
- [5] Hender T.C. et al 1992 Effect of resonant magnetic perturbations on COMPASS-C tokamak discharges *Nucl. Fusion* **32** 2091
- [6] Evans T.E. et al 2004 Suppression of large edge-localized modes in high-confinement DIII-D plasmas with a stochastic magnetic boundary *Phys. Rev. Lett.* **92** 235003
- [7] Liang Y. et al 2007 Active control of type-I edge-localized modes with $n = 1$ perturbation fields in the JET tokamak *Phys. Rev. Lett.* **98** 265004
- [8] Kirk A. et al (The MAST Team) 2010 Resonant magnetic perturbation experiments on MAST using external and internal coils for ELM control *Nucl. Fusion* **50** 034008
- [9] Wolfe S.M. 2005 Nonaxisymmetric field effects on alcator C-Mod *Phys. Plasmas* **12** 056110
- [10] Buttery R.J., Benedetti M.D., Hender T.C. and Tubbing B.J.D. 2000 Error field experiments in JET *Nucl. Fusion* **40** 807
- [11] Menard J.E., Bell M.G., Bell R.E., Fredrickson E.D., Gates D.A., Kaye S.M., LeBlanc B.P., Maingi R., Mueller D. and Sabbagh S.A. 2003 β -limiting MHD instabilities in improved-performance NSTX spherical torus plasmas *Nucl. Fusion* **43** 330
- [12] Park J.-K., Boozer A.H., Menard J.E. and Schaffer M.J. 2008 Error field correction in ITER *Nucl. Fusion* **48** 045006
- [13] Paz-Soldan C., Buttery R.J., Garofalo A.M., Hanson J.M., La Haye R.J., Lancot M.J., Park J.-K., Solomon W.M. and Strait E.J. 2014 The spectral basis of optimal error field correction on DIII-D *Nucl. Fusion* **54** 073013
- [14] Menard J.E. et al 2017 Overview of NSTX Upgrade initial results and modelling highlights *Nucl. Fusion* **57** 102006
- [15] Battaglia D.J. et al 2018 Scenario development during commissioning operations on the national spherical torus experiment upgrade *Nucl. Fusion* **58** 046010
- [16] NSTX-U centerstack https://nstx.pppl.gov/DragNDrop/Presentation_Template/NSTX-U_centerstack-fullview.jpg accessed April 12 2019
- [17] Menard J.E. et al (The NSTX Team) 2012 Overview of the physics and engineering design of nstx upgrade *Nucl. Fusion* **52** 083015
- [18] La Haye R.J. and Scoville J.T. 1991 A method to measure poloidal field coil irregularities in toroidal plasma devices *Rev. Sci. Instrum.* **62** 2146
- [19] Buttery R.J. et al (JET Team, COMPASS-D Research Team and DIII-D Team) 1999 Error field mode studies on JET, COMPASS-D and DIII-D, and implications for ITER *Nucl. Fusion* **39** 1827
- [20] Park J.-K., Boozer A.H. and Glasser A.H. 2007 Computation of three-dimensional tokamak and spherical torus equilibria *Phys. Plasmas* **14** 052110
- [21] Schaffer M.J., Menard J.E., Aldan M.P., Bialek J.M., Evans T.E. and Moyer R.A. 2008 Study of in-vessel nonaxisymmetric ELM suppression coil concepts for ITER *Nucl. Fusion* **48** 024004
- [22] Park J.-K., Boozer A.H. and Menard J.E. 2008 Spectral asymmetry due to magnetic coordinates *Phys. Plasmas* **15** 064501

- [23] Boozer A.H. 2001 Error field amplification and rotation damping in tokamak plasmas *Phys. Rev. Lett.* **86** 5059
- [24] Ferraro N.M. 2012 Calculations of two-fluid linear response to non-axisymmetric fields in tokamaks *Phys. Plasmas* **19** 056105
- [25] Scoville J.T. and La Haye R.J. 2003 Multi-mode error field correction on the DIII-D tokamak *Nucl. Fusion* **43** 250
- [26] Gerhardt S.P. 2017 Currents for inner PF error field assessments NSTX-U Memo MAG-171010-SPG-2
- [27] Park J.-K. and Logan N.C. 2017 Self-consistent perturbed equilibrium with neoclassical toroidal torque in tokamaks *Phys. Plasmas* **24** 032505
- [28] Munaretto S., Evans T.E., Ferraro N.M., Orlov D.M., Trevisan G.L. and Wu W. Assessment of equilibrium field coil misalignments on the divertor footprints in NSTX-U *Nucl. Fusion*. **59** 076039
- [29] Bialek J., Boozer A.H., Mauel M.E. and Navratil G.A. 2001 Modeling of active control of external magnetohydrodynamic instabilities *Phys. Plasmas* **8** 2170
- [30] Sontag A.C., Sabbagh S.A., Zhu W., Menard J.E., Bell R.E., Bialek J.M., Bell M.G., Gates D.A., Glasser A.H. and LeBlanc B.P. 2007 Investigation of resistive wall mode stabilization physics in high-beta plasmas using applied non-axisymmetric fields in NSTX *Nucl. Fusion* **47** 1005